Supplementary Information for

Morphological growth dynamics, mechanical stability, and active microtubule mechanics underlying spindle self-organization

Tatsuya Fukuyama[1,2], Lucan Yan[1], Masahito Tanaka[3], Megumi Yamaoka[3], Kei Saito[3], Shih-Chieh Ti[4], Chung-Chi Liao[5,6], Kuo-Chiang Hsia[5,6], Yusuke T. Maeda[1,*], and Yuta Shimamoto[3,7,*]

[1]Department of Physics, Faculty of Science, Kyushu University, Fukuoka 819-0395, Japan
[2]Theoretical Biology Group, The Exploratory Research Center on Life and Living Systems, National Institute of Natural Sciences, Okazaki 444-8787, Japan
[3]Department of Chromosome Science, National Institute of Genetics, Shizuoka 411-8540, Japan
[4]School of Biomedical Sciences, The University of Hong Kong, Hong Kong SAR, China
[5]Institute of Molecular Biology, Academia Sinica, Taipei 115, Taiwan
[6]Molecular and Cell Biology, Taiwan International Graduate Program, Academia Sinica, Taipei 115, Taiwan
[7]Department of Genetics, Sokendai University, Shizuoka 411-8540, Japan
[*]Correspondence: ymaeda@phys.kyushu-u.ac.jp (Y.T.M.); yuta.shimamoto@nig.ac.jp (Y.S.)

This PDF file includes:

Other supplementary materials for this manuscript include the following:

Movies S1 to S9

Extended Materials and Methods

Preparation of cytoplasmic extracts

The cytoplasmic extracts used in this study were prepared from unfertilized *X. laevis* eggs according to the previously described method (1). For each preparation, 2–3 female frogs were primed with progesterone (HOR-272, ProSpec) and induced to ovulate using human chorionic gonadotropin (CG-10, Sigma). Following 16–18 h of the gonadotropin injection, laid eggs with normal morphologies were pooled and washed with MMR (5 mM Na-HEPES, 0.1 mM EDTA, 100 mM NaCl, 2 mM KCl, 1 mM $MgCl_2$, and 2 mM $CaCl_2$, pH 7.7). The washed eggs were then treated with 2% cysteine for 6–9 min and thoroughly rinsed with buffers in the following order: XB (10 mM K-HEPES, 100 mM KCl, 1 mM $MgCl_2$, 0.1 mM $CaCl_2$, and 50 mM sucrose; pH 7.7), CSF-XB (XB plus 1 mM $MgCl_2$ and 5 mM EGTA), and CSF-XB + PI (CSF-XB plus 10 µg/ml each of leupeptin, pepstatin A, and chymostatin). The rinsed eggs were then transferred to centrifuge tubes (344057, Beckman) containing cytochalasin D (10 µg/ml final concentration), packed using a tabletop centrifuge by two spin cycles (5702R, Eppendorf), and then crushed by centrifugation in an SW-55 rotor at 10,000 ×*g* for 15 min at 16°C (XE-90, Beckman Coulter). Finally, the cytoplasmic fraction of the crushed eggs was retrieved using 16-gauge needles and supplemented with Energy mix (75 mM creatine phosphate, 1 mM ATP, and 1 mM $MgCl_2$), protease inhibitors, and cytochalasin D (10 µg/ml). The entire procedure was performed in a temperature-controlled room at 19 ± 1°C. The prepared extracts were stored on ice and used within 6 h of preparation.

Spindle assembly and imaging

For spindle assembly, extracts prepared as above and arrested by cytostatic factor (CSF), were mixed with demembranated sperm (800 nuclei/µl) in 1.5 ml test tubes (Eppendorf) and released into interphase by the addition of $CaCl_2$ at a final concentration of 0.4 mM. Following a 90 min incubation at 18°C, each reaction was cycled back into the mitotic phase by dilution with an equal volume of CSF extracts with no added sperm and $CaCl_2$. Immediately after dilution, the reaction was supplemented with X-rhodamine-labeled tubulin and SYTOX Green (S7020, Thermo) at final concentrations of 200 nM and 1 nM, respectively, and then sandwiched between a clean glass slide and an 18 × 18 mm coverslip before sealing with VaLaP (1). The volume of the sealed reaction was 5 µl so that it could limit the sample thickness (~20 µm) and minimize the spindles' out-of-

focus drift and three-dimensional rotation. Finally, the slide was placed on the motorized sample stage (MS-2000, ASI) of an inverted microscope (Ti, Nikon) and imaged with a 20× objective lens (Plan Apo, 0.75NA, Nikon), a spinning-disk confocal unit (CSU-X1, Yokogawa) with two excitation lasers (OBIS 488 and 561, Coherent), and an sCMOS camera (Neo4.1, Andor). Time-lapse imaging was performed at 1 min intervals (exposure time: 50 ms for SYTOX™ green and 500 ms for X-rhodamine tubulin), controlled using a laser controller (1173961, Coherent) and image acquisition software (NIS-Elements, ver. 4.5, Nikon). To track multiple spindle assembly processes in parallel, the sample was raster-scanned using the Large Image function equipped with the software (scan area: 6 × 5 squares or 2.7 × 2.3 mm^2). The total time-lapse duration was 60–80 min, within which the spindle shape morphologies reached a steady state. Fluorescent speckle imaging was performed using the same microscope setup as above, but with the following modifications: (i) the objective lens used was 100× (Plan Apo TIRF, 1.49NA, Nikon), (ii) single-area images were acquired instead of raster-scan, (iii) the time interval was set at 1.5 s, and (iv) dye-labeled tubulins added were 30 nM. The assays were performed in a temperature-controlled room at 19 ± 1°C. In some cases, spindle images were intermittently distorted, in which case these data were excluded from subsequent analyses.

Micromanipulation

Spindle micromanipulation was performed using a pair of glass microneedles (diameter: 1–2 μm) prepared by fabricating glass rods (G-1000, Narishige) using a capillary puller (PD-10, Narishige) and a microforge (MF200, World Precision Instruments) (2). For each experiment, extracts containing pre-assembled spindles were placed in an open imaging chamber assembled from a coverslip and an aperture-rubber plate (2) and then covered with mineral oil. A spindle of typical size and shape was then searched for by moving the sample stage and then captured by inserting the tips of the microneedles near its pole. The insertion was such that the distance between the two microneedle tips was maintained at 2–3 μm and their positions were nearly symmetrical to the pole-to-pole axis of the spindle. Finally, the microneedles were separated to deform and split the pole, and the subsequent morphological changes of the spindle were recorded. The movement of the microneedles was controlled using three-axis hydraulic micromanipulators (MHW-3, Narishige). The shaft of the microneedles was bent using a micro-torch so that the approach angle of their tips was nearly perpendicular to the coverslip surface. A 60× (Plan Apo, 1.20NA, Nikon)

or 100× objective lens (Plan Apo TIRF, 1.49NA, Nikon) was used for the imaging. The interval of the time-lapse was set to 1 s.

Protein preparation

Recombinant augmin holocomplex was prepared by modification of our previously established strategy of using a baculovirus-insect cell protein expression system for better efficiency and higher protein yield (3). cDNA sequences encoding human Ccdc5 (NP_612452.1), Dgt3 (NP_001290072.1), Dgt5 (NM_015302.1), Dgt6 (NP_060115.3), C14orf94 (NM_017815.1), UCHL5IP (NP_059988.3), Cep27 (NP_060567.1), and Hice1 (AAH04398) were cloned into a single pACEBac1 vector. We fused the 5' end of the Dgt6 cDNA sequence to a nucleotide sequence (from 5' to 3') encoding a ZZ tag and two Tobacco Etch Virus (TEV) protease sites, and the 5' end of the Cep27 cDNA sequence was fused to a nucleotide sequence encoding green fluorescent protein (GFP). We then generated recombinant baculoviruses following the Bac-to-Bac method (Thermo). High Five cells at a density of 3.0–3.5 × 10^6 cells/mL in a volume of 2.4 L were infected with 1% (v/v) P3 viral stocks. The cells were harvested at ~60 h post-infection. The following purification steps were carried out on the ice or at 4°C. The cells were lysed in 80 ml lysis buffer (50 mM phosphate, 300 mM KCl, 5% (w/v) sucrose, 0.1% Tween-20, 1 mM β-mercaptoethanol, 3 U/ml Benzonase, and 1× Roche Complete EDTA-free protease inhibitor; pH 7.4) by Dounce homogenization (20 strokes), and the extract was clarified at 55,000 rpm in a Type 70 Ti rotor (Beckman Coulter) for 1 hour. The supernatant was then passed through a 0.22 μm Millex-GP PES membrane (Millipore SLGPR33RB) and loaded onto a 1 ml Rabbit IgG column pre-equilibrated with the lysis buffer. After being washed with 30 ml of lysis buffer, the UV (280 nm) absorption reached the baseline, and the columns were ready for elution by in-column TEV digestion. One milliliter of TEV solution (0.8 mg/mL in lysis buffer) was loaded onto the IgG column, followed by a 2 h incubation. The eluted protein solution was pooled and dialyzed against 500 ml of the concentrating buffer (1X BRB80, 100 mM KCl, 40% (w/v) sucrose, and 3 mM β-mercaptoethanol; pH 6.8) for 2 h. The concentrated protein was collected and loaded onto a Superose 6 10/300 column (Cytiva #29091596) equilibrated in size-exclusion buffer (1X BRB80, 10% (w/v) sucrose, 100 mM KCl, and 3 mM β-mercaptoethanol; pH 6.8). Followed by Coomassie blue-stained SDS-PAGE analysis, the concentration of the peak fractions was determined by

Bradford assay using BSA standards before being snap-frozen in liquid nitrogen and stored at −80°C.

The constitutively active Ran mutant was prepared by cloning the RanQ69L sequence (original sequence: NM_006325) into a modified pET28 expression vector with a 6× histidine tag and PreScission cleavage site at the N-terminus, and it was then expressed in an *E. coli* Rosetta strain (Novagen) with 0.5 mM IPTG for 16 h at 18°C. The harvested cells were resuspended in lysis buffer (50 mM potassium phosphate buffer, 150 mM NaCl, and 3 mM β-mercaptoethanol; pH 7.4) and lysed using M110P Microfluidizer, and the cell lysate was then centrifuged at 15,000 ×g for 30 min at 4°C. The supernatant was collected and incubated with Ni-NTA beads (QIAGEN) for 30 min, and the beads then were K-packed into a column. The column was first prewashed with buffer containing 50 mM potassium phosphate buffer (pH 7.4), 150 mM NaCl, 3 mM β-mercaptoethanol, and 25 mM imidazole. The protein was then eluted using 250 mM imidazole. The eluted protein fractions were collected and dialyzed against buffer (20 mM HEPES, 150 mM NaCl, and 3 mM DTT; pH 7.4) overnight at 4°C in the presence of PreScission protease for His-tag cleavage. After dialysis, the protein was further purified by ion-exchange chromatography using a HiTrap Q HP (5 ml) column. The proteins were eluted with buffer containing 20 mM HEPES (pH 7.4), 250 mM NaCl, and 3 mM DTT. The protein samples were then concentrated and purified by size-exclusion chromatography (Superdex 75 16/60) with buffer (20 mM HEPES, 150 mM NaCl, and 3 mM DTT; pH 7.4). The peak fractions were analyzed by SDS-PAGE. The eluted protein samples were concentrated, frozen in liquid nitrogen, and then stored at −80°C.

EB1-EGFP was prepared by cloning out the corresponding sequence from a plasmid vector (human EB1 in pEGFP N1 to express EB1-GFP (JB131); Addgene #39299) and inserting it into a pET28 expression vector using In-Fusion (Takara) with a 6× histidine tag at the N-terminus. The protein was expressed using *E.coli* Rosetta pLysS (70956, Novagen) cultured in LB and 100 ng/ml carbenicillin with 0.1 M IPTG at 37°C for 3 h. The cells were collected at 16,000 ×g for 20 min at 4°C and then resuspended in BugBuster reagent (Qiagen) for lysis. Following centrifugation of the lysed cells at 25,000 ×g for 20 min, the supernatant was batch bound to Ni-NTA agarose magnetic beads (36113, Qiagen) at 4°C for 1 h, washed three times with wash buffer (50 mM potassium phosphate buffer, 300 mM NaCl, 20 mM Imidazole, pH 8.0), and then subjected to protein elusion with elution buffer (50 mM potassium phosphate buffer, 300 mM NaCl, 250 mM Imidazole, pH 8.0) according to the manufacturer's protocol. Protease inhibitor cocktail (1860932, Thermo) and

0.05% Tween-20 were added to buffers throughout the preparation. The eluted protein was buffer-exchanged twice with CSF-XB using an Amicon filter device (30-K, Qiagen) spun at 14,000 ×g for 20 min at 4°C before being snap-frozen in liquid nitrogen and stored at −80°C.

Molecular perturbation

Monastrol (M505750, Toronto Research Chemicals) was added to extracts at the start of spindle assembly at a final concentration of 20 μM or 200 μM with 0.5% (v/v) DMSO. Purified augmin was added to extracts at the start of spindle assembly at a final concentration of 56 nM. A mock control was performed in parallel with each spindle assembly reaction and no noticeable influence on spindle shape morphologies was observed.

Microtubule nucleation assay

The branching microtubule nucleation assay (Fig. S9A−D) was performed in extracts to which RanQ69L, GFP-tagged EB1, and vanadate were added (4). First, freshly prepared CSF extracts were mixed on ice with X-rhodamine-labeled tubulin, EB1-GFP, and sodium orthovanadate (S6508, Sigma) to final concentrations of 77 nM, 13 nM, and 1 mM, respectively. RanQ69L was then added to the mixture at a final concentration of 7.5 μM along with either augmin holocomplex (at a final concentration of 56 nM) or control buffer (CSF-XB) and sealed in an imaging chamber comprising a KOH-washed glass slide and a coverslip (volume: 5 μl) for total internal reflection fluorescence imaging at room temperature. RanQ69L and augmin were prepared as 20× stocks and added to extracts. Labeled tubulin, EB1-GFP, and orthovanadate were added at 1 in 100 dilutions. Image acquisition was performed using NIS-Elements software (ver. 4.51, Nikon) with a 100× objective lens (1.49 NA, Nikon), fluorescence filters (#49002, Chroma), an excitation laser (488 nm; OBIS, Coherent) and an EMCCD camera (iXon Ultra, Andor) with a 50 ms exposure at 1 s intervals.

Data Analysis

Spindle shape morphology

The morphological growth dynamics of spindles were analyzed by processing time-lapse image data acquired in the X-rhodamine channel. Each image was first processed to reduce background noise using the Image J toolbox (CSBDeep; https://csbdeep.bioimagecomputing.com) (5) and then

binarized using a self-written MATLAB code (6). The binarization threshold was determined using the Otsu method (7). The spindle's centroid position was then determined in the binarized image, and an outline tracing vector, denoted as $R(\theta)$, was drawn from the centroid to the spindle contour so that the spindle's shape profile could be obtained as a function of angle θ ($-180° \leq \theta \leq 180°$) (see Fig. 2A). Finally, the shape profile obtained was decomposed into discrete Fourier modes according to the following equation:

$$R(\theta) = \sum_{n=0}^{+\infty} C_n e^{-in\theta} \quad \text{[Eq. 1]}$$
$$(n = 0,2,3 \ldots \ -\pi \leq \theta \leq \pi).$$

where the integer n represents the structure's $n^{\text{-th}}$ order symmetry. For example, $n = 2$ corresponds to second-order symmetry and indicates the degree of the structure's bipolarity; $n = 3$ corresponds to third-order symmetry and indicates the structure's degree of multipolarity. A structure with any shape deviation from the right symmetry yielded a combination of $n^{\text{-th}}$ order symmetries. The first-order symmetry ($n = 1$) was always zero because the vector $R(\theta)$ originated from the spindle's centroid. The amplitude of each Fourier mode, C_n, was calculated as follows:

$$C_n = \frac{1}{2\pi} \int_{-\pi}^{\pi} R(\theta)\, e^{in\theta}\, d\theta \quad \text{[Eq. 2]}$$
$$(n = 0,2,3 \ldots \ -\pi \leq \theta \leq \pi).$$

In most cases, the initial three components ($n = 0, 2, 3$) were sufficient to reconstitute the original spindle shape, and the higher modes ($n \geq 4$) were negligibly small. Hence, the following analyses were performed by focusing on C_2 and C_3. To generate morphological growth trajectories of spindles (Fig. 2C–E, Fig. 5B, E, I, L), the values of C_2 and C_3 were calculated at each time point (t) of their individual time-lapse, normalized by C_0 for size scaling (denoted as $\widetilde{C_2}$ and $\widetilde{C_3}$, respectively), and plotted in a two-dimensional plane composed of $\widetilde{C_2}$ and $\widetilde{C_3}$.

The cross-correlation between $\widetilde{C_2}$ and $\widetilde{C_3}$ was calculated using the following equation:

$$Cr(\Delta t) = \frac{\langle \tilde{C}_2(t) - \langle \tilde{C}_2 \rangle \rangle \cdot \langle \tilde{C}_3(t+\Delta t) - \langle \tilde{C}_3 \rangle \rangle}{\sqrt{\langle (\tilde{C}_2(t) - \langle \tilde{C}_2 \rangle)^2 \rangle \langle (\tilde{C}_3(t) - \langle \tilde{C}_3 \rangle)^2 \rangle}} \quad \text{[Eq. 3]}$$

where t is the absolute time and Δt is the time difference between $\widetilde{C_2}$ and $\widetilde{C_3}$. The profile of the cross-correlation was generated as a function of Δt for individual spindle samples and then averaged to create the graphs provided (Fig.2, I–K). A positive time difference indicates the precedence of $\widetilde{C_2}$ over $\widetilde{C_3}$.

The classification of spindle time-lapse data by machine learning was performed based on the Linear Discriminant Analysis (LDA) model (8), which was executed using custom-made MATLAB code (9). The model was first trained with 200 representative still images of spindles, which were acquired independently from time-lapse experiments. Each training image was manually labeled with one of the following shape classes: circular (n = 40), bipolar (n = 80), or multipolar (n = 80). The values of $\widetilde{C_2}$ and $\widetilde{C_3}$ were then calculated for each training image and linked to the string of the labeled shape class. All the training image data were then mapped onto a single coordinate plane of $\widetilde{C_2} - \widetilde{C_3}$, whereby the model defined the borders between different shape classes and created a phase map, which was used to discriminate spindle images based on the combination of ($\widetilde{C_2}$, $\widetilde{C_3}$). Next, the trained model was tested using 100 spindle still images prepared separately from the training data set. Finally, spindle time-lapse data, used for generating morphological growth trajectories, were sorted based on their matured shape morphologies. The sorting was made by locating the final destination of each trajectory on the phase map. Another analysis model (Quadratic Discriminant Analysis or QDA) was used to analyze the same dataset, which yielded essentially the same outcome (Fig. S4B).

The probability density of the spindle's growth trajectories (Fig. 2F–H; Fig. 5C, F, J, M) was calculated as follows. First, within each spindle shape class defined as above, all trajectory data were pooled and projected onto a single coordinate plane composed of $\widetilde{C_2}$ and $\widetilde{C_3}$. Then, the number of trajectory segments that passed at each coordinate point ($\widetilde{C_2}, \widetilde{C_3}$) was counted and normalized by the total number of segments in all the trajectories projected. Finally, the normalized two-dimensional histogram was displayed as a heat map with warmer colors representing higher trajectory densities. The analysis was performed using MATLAB with the function "ksdensity."

DNA amount and DNA distribution in the spindle

The amount of DNA in each spindle (M_{DNA}) (Fig. S5A) was measured by analyzing the fluorescence signal intensity of the SYTOX Green dye, according to the following equation:

$$M_{DNA} = I_{sp} - \left(\left(I_{bg} - I_{sp}\right)/\left(S_{bg} - S_{sp}\right)\right) \times S_{sp} \quad \text{[Eq. 4]}.$$

where I_{sp} is the integrated fluorescence intensity within a square ROI drawn to cover the spindle (65×65 μm^2), and I_{bg} is the integrated fluorescence intensity within another ROI drawn to cover the first ROI (80×80 μm^2). S_{sp} and S_{bg} are the areas of the two ROIs, respectively. The values obtained were normalized by the mean background fluorescence measured for each extract preparation, pooled within each spindle shape class, and then plotted in the graphs presented. The distribution of DNA in each spindle (Fig. S5B) was analyzed by generating an intensity profile of the SYTOX signal in the polar coordinate for which the origin was set to the spindle's centroid (see cartoon in Fig. S5B). The profile obtained was smoothened at each 1 μm bin along the coordinate axis and then a linear regression was performed to determine the slope of the profile. The slope values were pooled within each spindle shape class and plotted in the graphs presented.

Speckle tracking

Speckle tracking was performed using the particle-tracking plug-in in ImageJ (PTA) (10). First, successive time-lapse images of tubulin speckles, acquired over the course of spindle self-organization (interval:1.5 s), were cropped over -50 to 50 frames from the time point of interest and then processed for background noise reduction using self-written macros (11). The images were then loaded to the particle tracking plug-in so that individual speckles could be detected in each image and linked across adjacent images (analysis parameters: 2-D Gaussian fit, ROI Size: 15×15, nearest particle range: 0.75; other parameters were as default). Finally, the speckles that were successfully tracked over ≥ 10 frames were mapped in a single two-dimensional plane such that individual trajectories could be visualized (Fig. 3B). To color code the orientation of individual speckle movements, the mean angle of each speckle track was calculated over the five timepoint segments along the trajectory. An angle of 0° was defined as corresponding approximately to the structure's established bipolar axis. To split speckles based on their on- and off-axis movements (Fig. 3C), a vector was drawn from the start to the end point of each trajectory and the angle relative to the bipolar axis was obtained. Speckles with an absolute vector angle

between 45° and 135° were assigned as the off-axis fraction, and those with vector angles outside this range were assigned as the on-axis fraction.

Spindle deformation

The extent of spindle deformation induced by a pair of microneedles (Fig. 4) was measured by analysis of the X-rhodamine channel images. The distance between the edges of the structure deformed was measured at the time point at which the microneedles reached the maximal separation. The percentile degree of deformation was then calculated as the value relative to the initial spindle length, which was determined by measuring the pole-to-pole distance of the spindle prior to the stretch. The duration of hold was measured from the time point at which the microneedles reached a maximal separation to the time point at which one microneedle was withdrawn from the spindle. The symmetry of the micromanipulation procedure (*S*, in %) (Fig. S7B) was determined according to the following equation:

$$S = \{1 - |(x_1 - x_2)|/(x_1 + x_2)\} \times 100 \quad \text{[Eq. 5]}.$$

where x_1 and x_2 are the travel distances of the two microneedles from the start to the end of the micromanipulation procedure. A symmetrical movement of the two microneedles (i.e., $x_1 = x_2$) yields $S = 100\%$. An eccentric asymmetry moving only one microneedle (e.g., $x_2 = 0$) yields $S = 0\%$.

Microtubule branching

For the quantification of branching microtubule nucleation in the TIRF-based imaging assay (Fig. S9A–D), a triangular ROI that encompassed the root of the fan-like microtubule structure was placed and the integrated signal intensity within the ROI was measured using ImageJ. The ROI used was the same size (285 μm^2) and the corner angle (50°) for all the structures analyzed. Normalized intensities were obtained by dividing the signal intensities measured at each time frame by the one at the initial time frame.

Figures S1 to S9

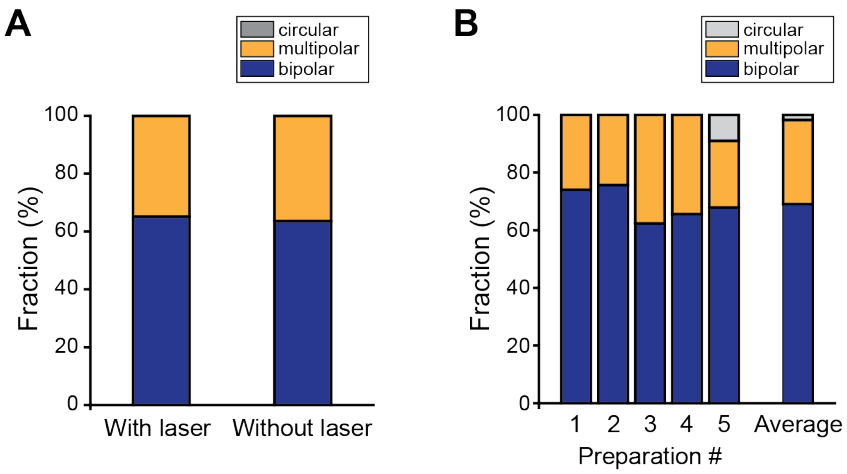

Figure S1. Validation of the time-lapse imaging assay. (**A**) Effect of laser excitation. The fraction percentages of the spindle shape phenotypes (circular, bipolar, and multipolar) were examined at 60 min from the start of spindle assembly in reactions performed in imaging chambers with and without laser excitation of our standard time-lapse condition (1 s intervals, 500 ms exposure) (n = 66 and 88, respectively). (**B**) Variation among preparation batches. The fraction percentages of the spindle shape phenotypes (circular, bipolar, and multipolar) were examined at 60 min from the start of spindle assembly performed in imaging chambers with our standard time-lapse condition for extracts from five independent preparations (n = 69, 41, 85, 90, and 143, for preparations #1 to #5, respectively). The right-most column is the average of the pooled data. The fraction percentages obtained were comparable to those typically obtained with reactions in test tubes. The bar colors are as indicated.

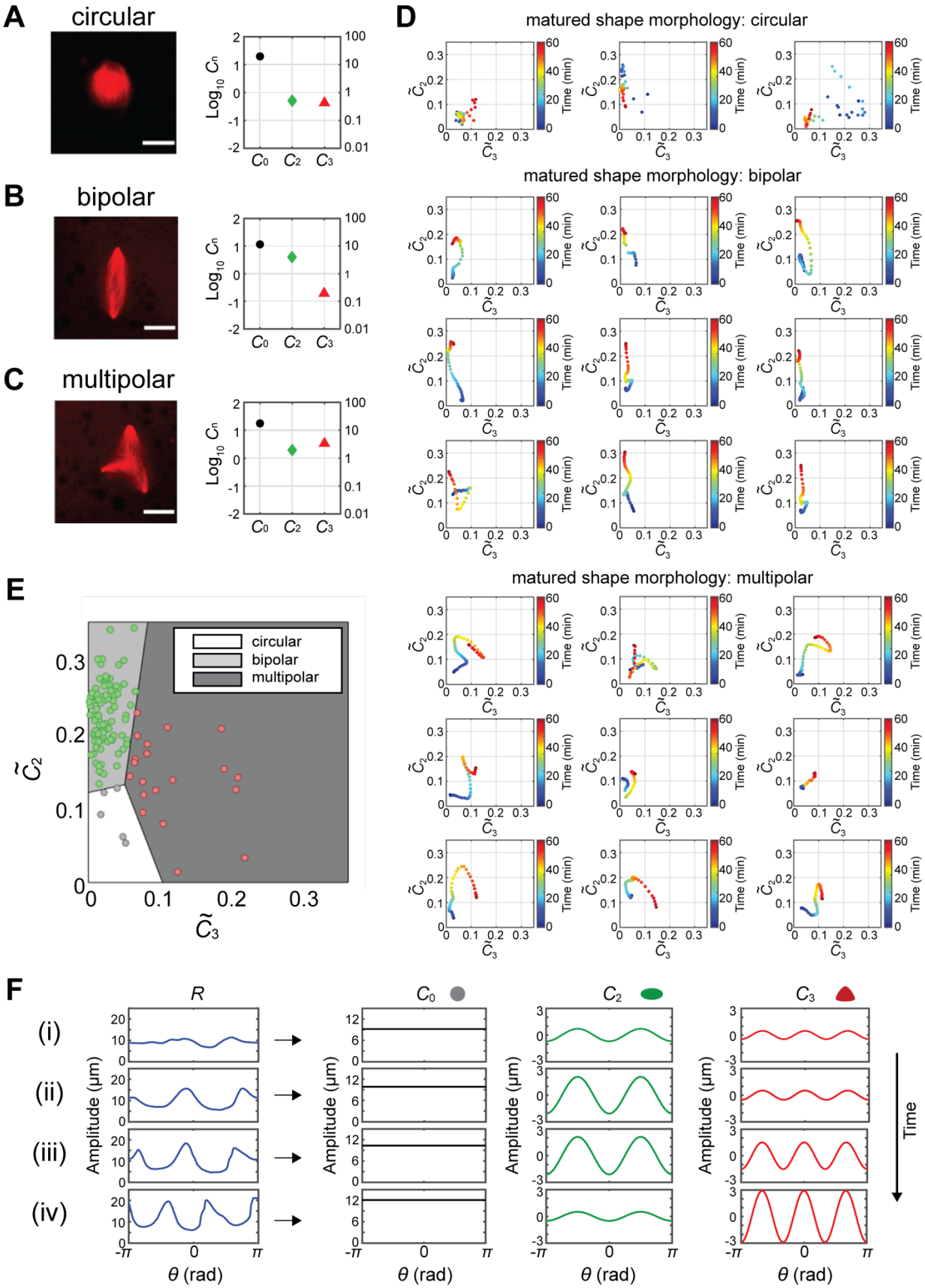
A
circular
B
bipolar
C
multipolar
Log10 Cn
C0 C2 C3
D
matured shape morphology: circular
matured shape morphology: bipolar
matured shape morphology: multipolar
Time (min)
E
circular
bipolar
multipolar
F
R
(i)
(ii)
(iii)
(iv)
Amplitude (μm)
θ (rad)
Time

Figure S2. Additional analysis data for the spindle's morphological growth dynamics. (**A–C**) Values of C_0, C_2, and C_3 acquired from representative images of circular (**A**), bipolar (**B**), and multipolar (**C**) structures as presented (pictures; Red, X-rhodamine tubulin). The Y-axis for each C_n value is logarithmic. Scale bars, 25 μm. (**D**) Other examples of morphological growth trajectories generated from multiple spindle time-lapse data. Each data was sorted into the three shape classes as indicated by inspection of the final shape morphologies in the last time-lapse frame. The graph presentation is as in Fig. 2C–E. Additional trajectory data are available in Figshare (total n = 145). (**E**) Phase map created by the machine learning-based algorithm employed for phenotype sorting. A total of n = 200 spindle still images were used for training to create the map. The performance of the trained algorithm was evaluated using n = 100 test spindle images prepared independently (colored plots). (**F**) Time-dependent changes of R, C_0, C_2, and C_3 obtained from an example spindle image in the inset of Fig. 2B undergoing multipolar self-organization. The plots relating to C_0, C_2, and C_3 indicate the $n^{\text{-th}}$ Fourier modes reconstructed with the function $C_n \cos(n\theta)$ (i = 0, 2, 3). The roman numerals correspond to those associated with each image in Fig. 2B. Note that the decomposed Fourier modes do not include phase arbitrariness.

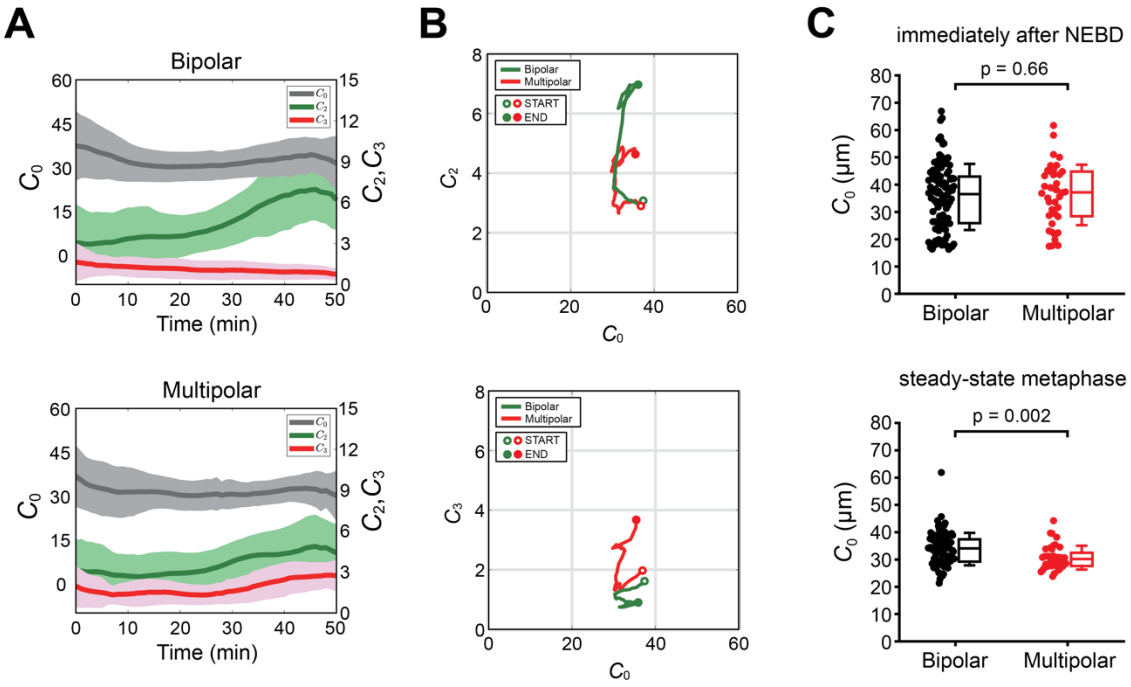

Figure S3. Relationships between spindle size and spindle shape. (**A**) Change over time of spindle size and shape. The time-dependent change of C_0 (gray; left vertical axis), the measure of the structure's size obtained as in Fig. 2A, is displayed along with the changes in the corresponding shape parameters C_2 and C_3 (green and red, respectively; right vertical axis). Solid lines indicate the means; colored areas are the SDs. (**B**) Trajectories of the spindle's shape growth with size. The time-dependent change of C_0 was plotted against those of C_2 and C_3 in the two-dimensional plane to compare the temporal growth dynamics of spindle size and shape between bipolar (green) and multipolar (red) spindles. The trajectories were distinctly different in their movements along the vertical (i.e., C_2 and C_3) axes in bipolar versus multipolar spindles. In contrast, the movements along the horizontal (i.e., C_0) axis were comparable. (**C**) Spindle size distribution by shape. The values of C_0 were plotted for bipolar and multipolar spindles immediately after nuclear envelope breakdown (upper panel) and at the steady-state metaphase (lower panel). Box plots represent the medians (horizontal lines) with inter-quartile ranges (boxes) and the SDs (whiskers) (n = 88 and 37, respectively). p, statistical significance values by Mann–Whitney *U*-test.

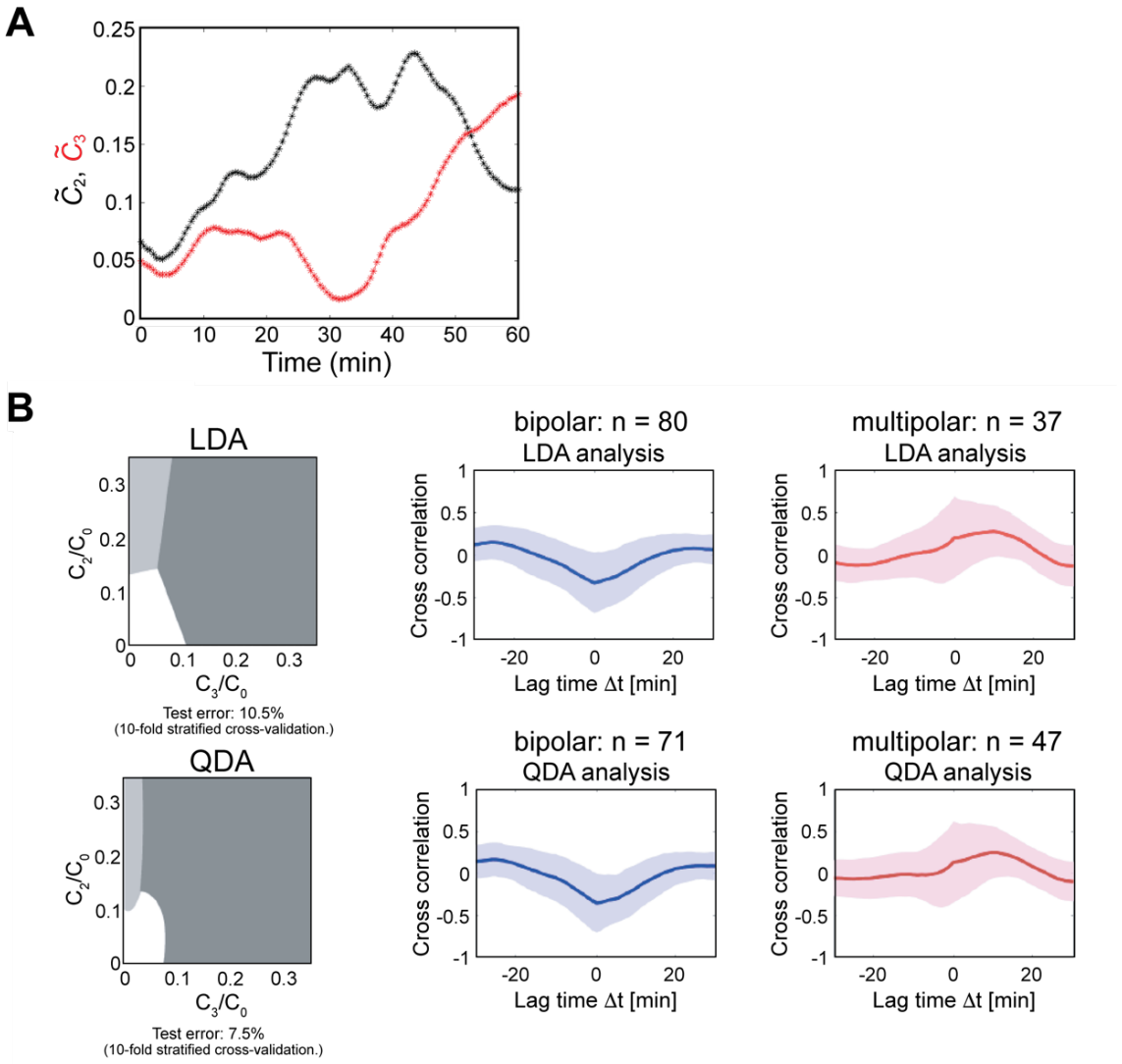

Figure S4. Additional data for the cross-correlation analysis. (**A**) Example time-courses of $\widetilde{C_2}$ and $\widetilde{C_3}$ obtained from a representative spindle time-lapse data. A change of $\widetilde{C_2}$ and $\widetilde{C_3}$ in the same direction along the vertical axis yields a positive correlation; a change in the opposite direction yields a negative correlation. The cross-correlation value was calculated over the entire time period while shifting the two time-course profiles one over the other along the horizontal axis. (**B**) Comparison of the machine learning models. Linear Discriminant Analysis (LDA) and Quadratic Discriminant Analysis (QDA) models were applied to the same data set, and the mean cross-correlation profiles were generated. Whereas the numbers of samples sorted to each spindle shape class differed slightly (~10%, as indicated at the top of each graph), due to the different border definitions in the phase map (left-most panels), the overall trends of the cross-correlation profiles (e.g., peak position and direction) were maintained.

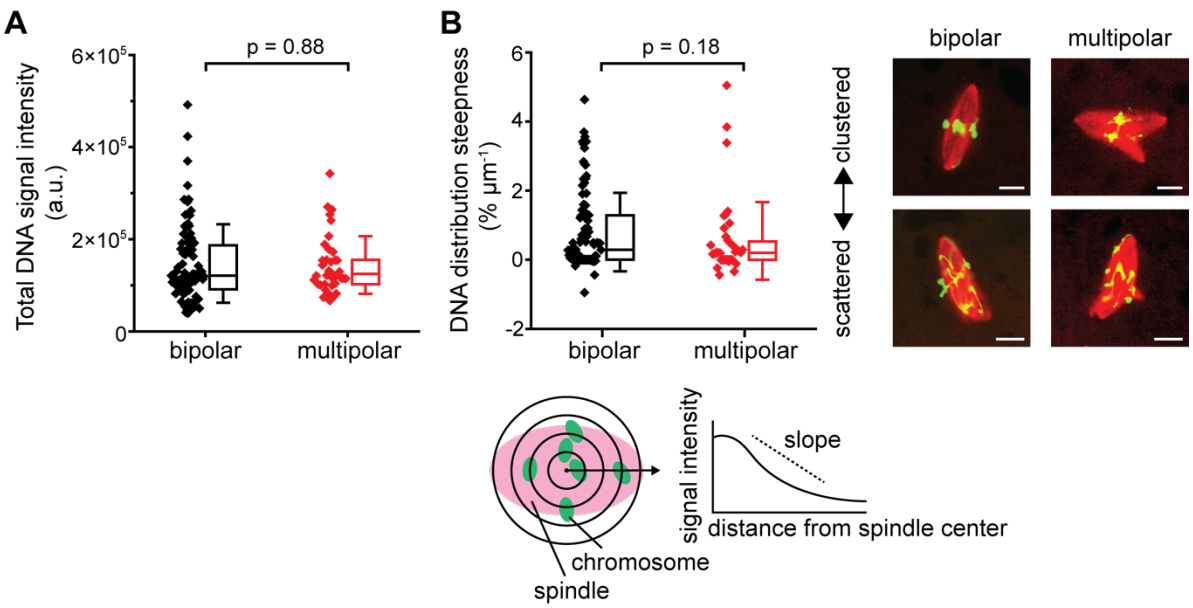

Figure S5. The amount and distribution of DNA in bipolar and multipolar spindles. (**A**) DNA amount. The total fluorescence signal intensity of DNA was measured for each spindle and divided into the two indicated columns based on the assigned spindle shape phenotype (n = 145). (**B**) DNA distribution. The distribution of DNA across the spindle was analyzed by generating a polar coordinate intensity profile and calculating the slope of the profile by linear regression (n = 145). The slope value indicates the percentile decrease of the DNA signal intensity per unit length; a larger value represents more clustered DNA around the equator. Representative images of clustered and scattered DNA organizations for bipolar and multipolar spindles are also provided to the right of the graph. Red, tubulin; Green, DNA. Scale bars, 10 µm. Box plots represent the medians (horizontal lines) with inter-quartile ranges (boxes) and the SDs (whiskers). p, statistical significance values by Mann–Whitney *U*-test.

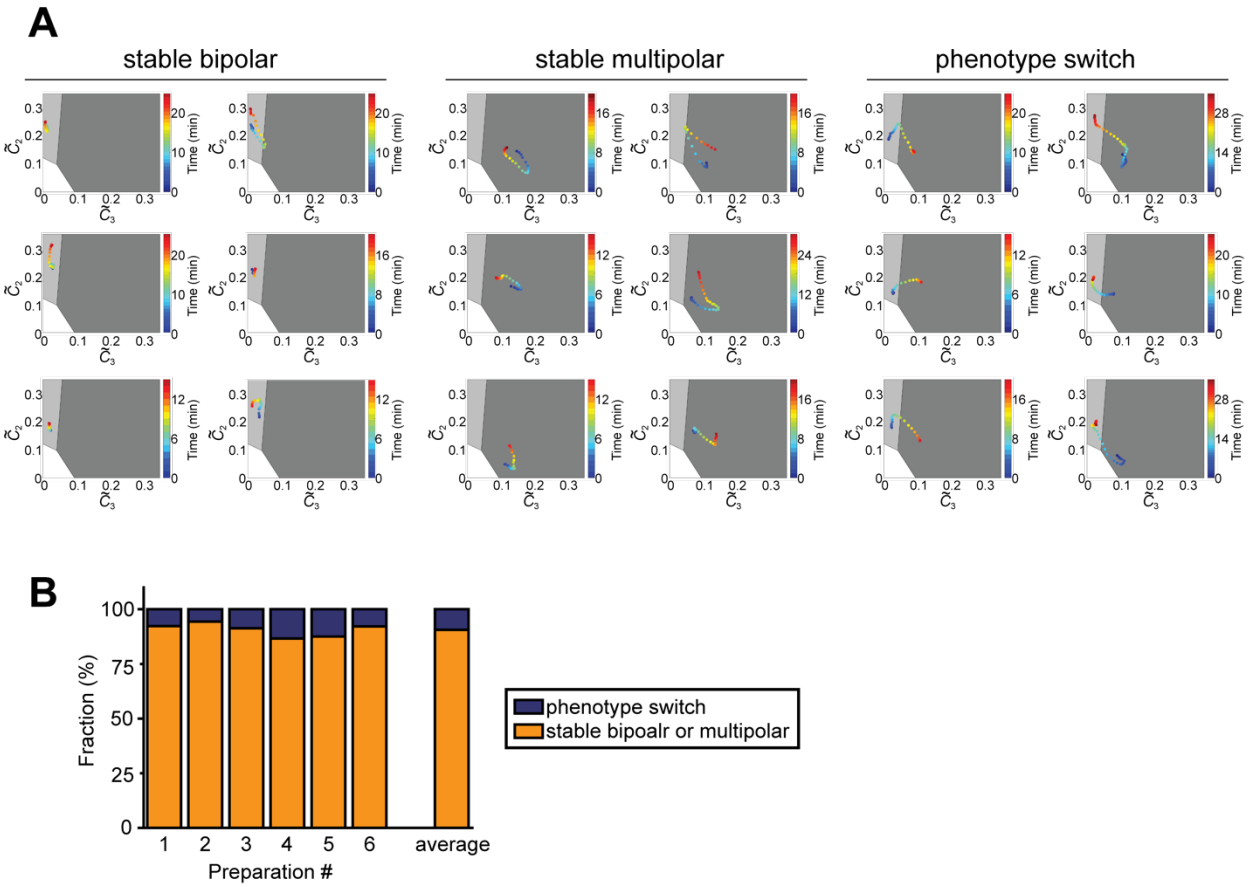

Figure S6. Morphological stability of spindles at the steady-state. (**A**) Spindle's steady-state shape stability was examined by generating the $\widetilde{C_2}$–$\widetilde{C_3}$ trajectories on the shape classification phase map (Fig. S2E) at > 60 min from the start of self-organization (total n = 245). Examples of the following three representative cases (six for each case) are shown: (i) stable bipolar, (ii) stable multipolar, and (iii) interconversion between bipolar and multipolar. For stable bipolar and stable multipolar cases, the trajectories stayed within the same-colored area in the phase map. For interconversion cases, the trajectories traveled across the border. Additional trajectory data are available in Figshare. (**B**) Probability of morphological stability and transformation at the steady-state. The analysis in (**A**) was performed with six independent extract preparations, and the number of structures that maintained the initial shape (orange) and those that converted either from bipolar to multipolar or from multipolar to bipolar (blue) were counted to calculate the fraction for each preparation (#1 to #6; total n = 13, 54, 23, 67, 24, and 64, respectively).

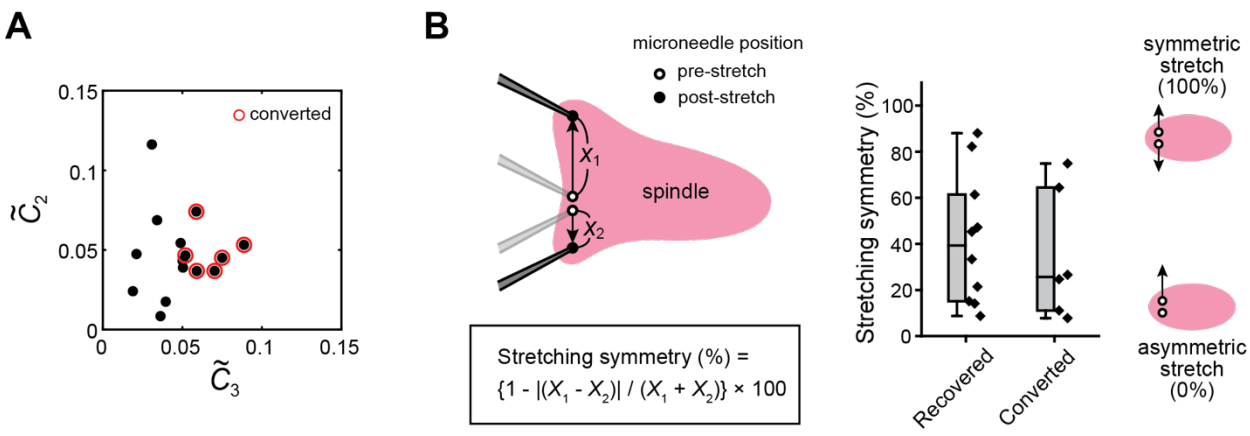

Figure S7. Additional data regarding the spindle micromanipulation experiments. (**A**) The values of $\widetilde{C_2}$ and $\widetilde{C_3}$ for each micromanipulated spindle at the maximal stretch. The spindles that converted to multipolar shapes following the microneedle withdrawal are circled in red. (**B**) Effect of the micromanipulation procedure on spindle shape stability. Schematic diagram shows a bipolar spindle (pink) for which the left-side pole is micromanipulated by a pair of microneedles (grey rods). The symmetry of the stretch, which varied for each spindle, was quantified by measuring the difference between the displacements of the two microneedle tips ($X_1 - X_2$) from pre-stretch (open circles) to post-stretch positions (filled circles) and scaling it to the total stretching distance ($X_1 + X_2$), as provided by the equation in the square box. The degree of the stretching symmetry as determined for each micromanipulated spindle was then plotted in the two separate columns depending on whether the structure recovered bipolarity or converted to a multipolar shape (right-side graph). Box plots represent the medians (horizontal lines) with inter-quartile ranges (boxes), as well as minima and maxima (whiskers). The data analyzed are identical to those in Figure 4 (n = 16).

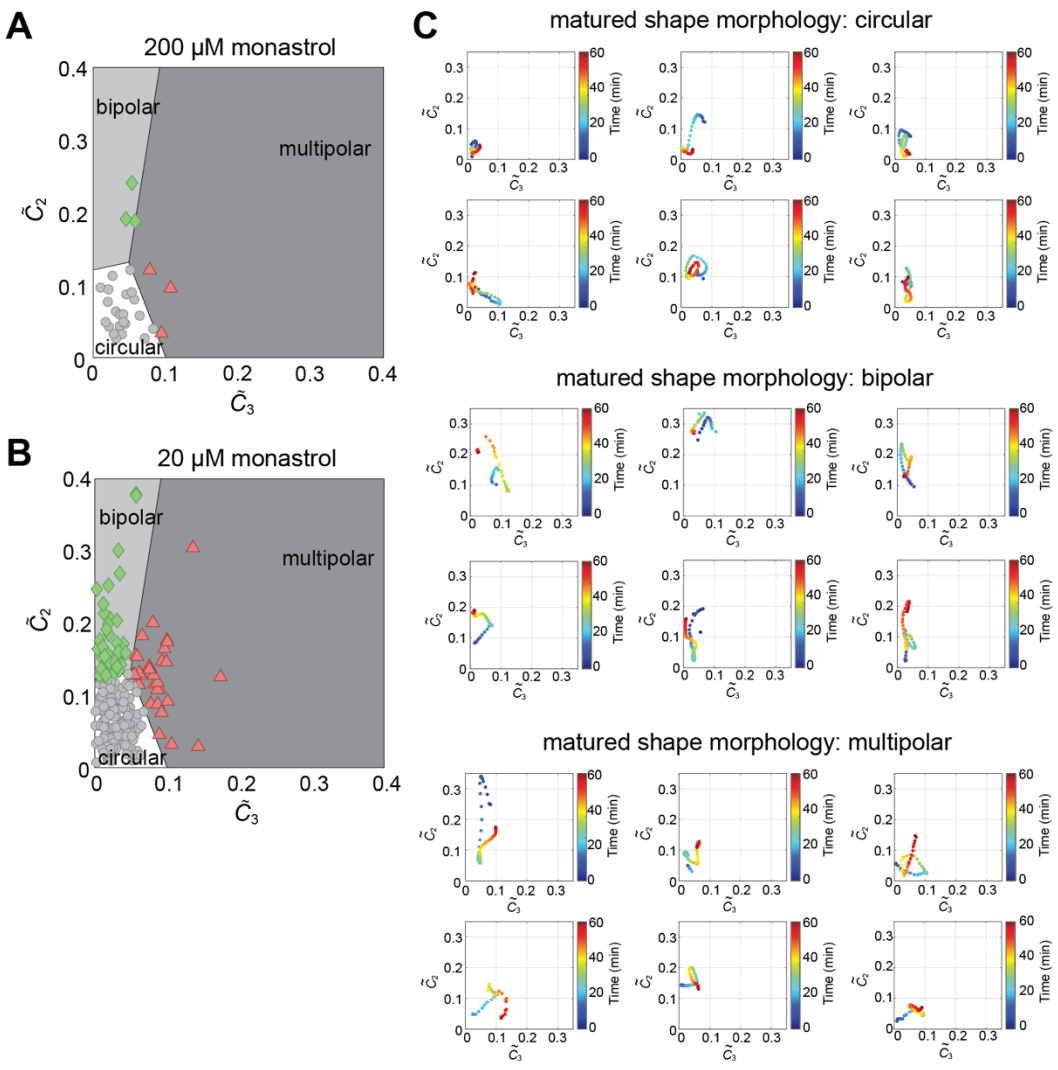

Figure S8. Additional kinesin-5 inhibition data. (**A, B**) Spindle shape phenotypes in the presence of 200 μM (n = 38) (**A**) and 20 μM (n = 215) monastrol (**B**). Individual spindle shapes at 60 min from the start of spindle assembly were analyzed and plotted as in Fig. S2E. (**C**) Additional examples of spindle's morphological growth trajectories obtained in the presence of 20 μM monastrol (total n = 215). Using the pre-trained machine learning model, the data were sorted into either of the three shape classes indicated. Additional trajectory data are available in Figshare.

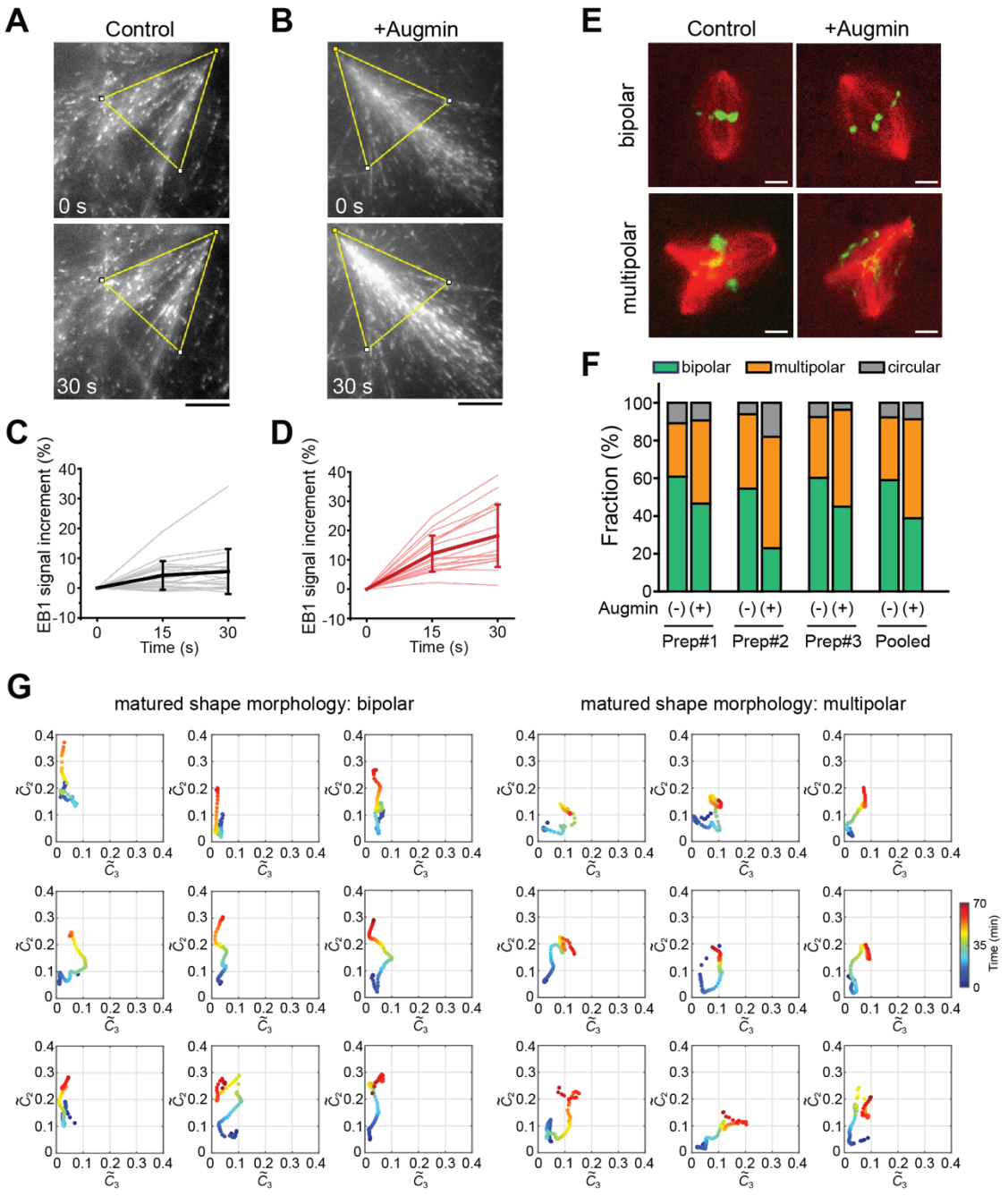

Figure S9. Effect of augmin on microtubule dynamics and spindle assembly phenotype. (**A-D**) Microtubule branching assay results. Extracts were supplemented with RanQ69L, EB1-GFP, and orthovanadate to promote microtubule branching in extracts and then imaged by TIRF-based microscopy. Representative images of EB1-GFP with buffer control (**A**) and 56 nM purified augmin holocomplex (**B**) are shown. The extent of the promoted nucleation was analyzed using the yellow triangular ROI indicated in each image, which was drawn to cover the fan-like

microtubule structure. The change in the total EB1-GFP signal intensity was measured over 30 s for the control (**C**) and with excess augmin (**D**) (n = 21 and 17, respectively). Scale bars, 10 μm. (**E, F**) Spindle assembly phenotype results. (**E**) Representative images of bipolar and multipolar spindles observed in extracts added with control buffer (left two panels) or 56 nM purified augmin holocomplex (right two panels). Red, tubulin; green, DNA. Scale bars are 10 μm. (**F**) The probability of bipolar and non-bipolar spindle formation examined at 60 min from the start of spindle assembly. The analysis was performed with three independent extract preparations (#1 to #3) each for control (n = 46, 66, and 171, respectively; labeled "(-)") and with purified augmin (n = 43, 83, and 160, respectively; labeled "(+)"). The two columns on the right are the pooled averages of each condition. (**G**) Additional examples of spindle's morphological growth trajectories obtained in the presence of excess augmin (total n = 172). Using the pre-trained machine learning model, the data were sorted into either of the three shape classes indicated. Additional trajectory data are available in Figshare.

Legends for the Movies

Movie S1 Time-lapse movie of bipolar spindle self-organization. An extract reaction, released into the mitotic phase with pre-assembled nuclei, was placed in an imaging chamber and imaged by confocal fluorescence microscopy. A structure maturing into bipolar shape while drifting across the chamber was tracked and cropped at each time-lapse frame to create the movie. Image size, 100 × 100 μm. Total movie duration, 70 min.

Movie S2 Time-lapse movie of multipolar spindle self-organization. A structure maturing into multipolar shape within the same extract as in Movie S1 was tracked and cropped at each time-lapse frame to create the movie. Image size, 100 × 100 μm. Total movie duration, 70 min.

Movie S3 Fluorescent speckle microscopy movie of a spindle imaged at its early growth phase. A structure maturing into tripolar shape was visualized using a low concentration of X-rhodamine tubulin for fluorescent speckle microscopy. Over time, the major bipolar axis gradually established approximately along the vertical axis of the image plane. In addition, an extra pole formed around the bottom-right part of the structure. The mass with a faint signal near the center of the structure is bleed-through from chromosomes labeled with another dye. Image size: 54 × 54 μm. Total movie duration, 15 min.

Movie S4 Time-lapse movie of a spindle undergoing bipolar shape recovery after micromanipulation. A bipolar spindle was captured by inserting the tips of the two microneedles near its left-side pole and then stretched to split the pole. One of the two microneedles (the upper one in the movie) was then withdrawn from the structure, while the other microneedle was left in place. The freed pole gradually coalesced into the main spindle body and the bipolar shape was restored. Image size: 73 × 60 μm. Total movie duration, 32.5 min.

Movie S5 Time-lapse movie of a spindle undergoing multipolar shape transformation after micromanipulation. A bipolar spindle was captured by inserting the tips of the two microneedles near its left-side pole and stretched to split the pole. One of the two microneedles (the upper one in the movie) was then withdrawn from the structure, while the other microneedle was left in place.

The freed pole remained in the new position such that the structure maintained its tripolar shape. Image size, 51 × 51 μm. Total movie duration, 19.3 min.

Movie S6 Another time-lapse movie of a spindle undergoing multipolar shape transformation after micromanipulation. The micromanipulation procedure, as shown in Movie S5, was performed at the upper pole of another bipolar spindle. Fluorescent tubulin was added at the speckle imaging condition. Image size, 47 × 47 μm. Total movie duration, 20 min.

Movie S7 Time-lapse movie of bipolar spindle self-organization in the presence of 20 μM monastrol. An extract reaction, released into the mitotic phase with pre-assembled nuclei and 20 μM monastrol, was placed in an imaging chamber and imaged by confocal fluorescence microscopy. A structure maturing into bipolar shape was tracked and cropped at each time-lapse frame to create the movie. Image size 100 × 100 μm. Total movie duration, 60 min.

Movie S8 Time-lapse movie of bipolar spindle self-organization in the presence of 56 nM augmin. An extract reaction, released into the mitotic phase with pre-assembled nuclei and 56 μM purified augmin holocomplex, was placed in an imaging chamber and imaged by confocal fluorescence microscopy. A structure maturing into bipolar shape was tracked and cropped at each time-lapse frame to create the movie. Image size 100 × 100 μm. Total movie duration, 70 min.

Movie S9 Time-lapse movie of multipolar spindle self-organization in the presence of 56 nM augmin. An extract reaction, released into the mitotic phase with pre-assembled nuclei and 56 μM purified augmin holocomplex, was placed in an imaging chamber and imaged by confocal fluorescence microscopy. A structure maturing into multipolar shape was tracked and cropped at each time-lapse frame to create the movie. Image size 100 × 100 μm. Total movie duration, 70 min.

SI References

1. A. Desai, A. Murray, T. J. Mitchison, C. E. Walczak, The use of Xenopus egg extracts to study mitotic spindle assembly and function in vitro. *Methods Cell Biol* **61**, 385-412 (1999).

2. Y. Shimamoto, T. M. Kapoor, Microneedle-based analysis of the micromechanics of the metaphase spindle assembled in Xenopus laevis egg extracts. *Nat Protoc* **7**, 959-969 (2012).

3. K. C. Hsia *et al.*, Reconstitution of the augmin complex provides insights into its architecture and function. *Nat Cell Biol* **16**, 852-863 (2014).

4. S. Petry, A. C. Groen, K. Ishihara, T. J. Mitchison, R. D. Vale, Branching microtubule nucleation in Xenopus egg extracts mediated by augmin and TPX2. *Cell* **152**, 768-777 (2013).

5. M. Weigert *et al.*, Content-aware image restoration: pushing the limits of fluorescence microscopy. *Nat Methods* **15**, 1090-1097 (2018).

6. Y. T. Maeda, J. Inose, M. Y. Matsuo, S. Iwaya, M. Sano, Ordered patterns of cell shape and orientational correlation during spontaneous cell migration. *PLoS One* **3**, e3734 (2008).

7. N. Otsu, Threshold Selection Method from Gray-Level Histograms. *IEEE Transactions on Systems, Man, and Cybernetics* **9**, 62-66 (1979).

8. Y. Guo, T. Hastie, R. Tibshirani, Regularized linear discriminant analysis and its application in microarrays. *Biostatistics* **8**, 86-100 (2007).

9. P. Markopoulos, Linear Discriminant Analysis with few training data. *ICASSP* (2017).

10. M. Yamada *et al.*, Rab6a releases LIS1 from a dynein idling complex and activates dynein for retrograde movement. *Nat Commun* **4**, 2033 (2013).

11. J. Takagi, R. Sakamoto, G. Shiratsuchi, Y. T. Maeda, Y. Shimamoto, Mechanically Distinct Microtubule Arrays Determine the Length and Force Response of the Meiotic Spindle. *Dev Cell* **49**, 267-278 e265 (2019).